Tectonophysics 747–748 (2018) 108–114

Contents lists available at ScienceDirect

Tectonophysics

journal homepage: www.elsevier.com/locate/tecto

The 2017 Mw 7.3 Sarpol Zahāb Earthquake, Iran: A compact blind shallow-dipping thrust event in the mountain front fault basement

Kejie Chen[a], Wenbin Xu[b,*], P. Martin Mai[c], Hua Gao[d], Lei Zhang[b], Xiaoli Ding[b]

[a] Division of Geological and Planetary Sciences, California Institute of Technology, Pasadena, CA 91125, USA
[b] Department of Land Surveying and Geo-Informatics, The Hong Kong Polytechnic University, Hong Kong, China
[c] Division of Physical Sciences and Engineering, King Abdullah University of Science and Technology, 23955 Thuwal, Saudi Arabia
[d] Faculty of Geomatics, East China University of Technology, Nanchang 330013, China

ARTICLE INFO

Keywords:
Zagros
Joint inversion
Mountain Front Fault
InSAR

ABSTRACT

The 12 November 2017 Mw 7.3 Sarpol Zahāb earthquake is one of the largest events to have occurred in the north-western Zagros fold-and-thrust belt during the instrumental period. We use teleseismic and synthetic aperture radar data to study the earthquake source parameters, rupture process and active tectonic characteristics of the event. We find that both data sets individually produce remarkably similar slip distribution, indicative of buried faulting that is consistent with the lack of significant surface rupture. Through the joint inversion of satellite radar and teleseismic data, we find that the rupture propagated rapidly (~3.2 km/s) and asymmetrically along strike to the south, but relatively slowly (~1.5 km/s) in the updip direction, and formed a single large-slip asperity with a peak slip value close to 5 m. Given the regional tectonic context of the distribution of known faults and lithologies, we suggest that the maximum slip is either located in the lowest sedimentary cover or the uppermost basement of the Mountain Front Fault.

1. Introduction

As one of the most seismically active thrust zones (Vernant et al., 2004), the Zagros fold-and-thrust belt (ZFTB) extends from western Iran to northern Iraq for ~1500-km-long. The ZFTB accommodates one third of the total N–S Arabia-Eurasia continental collision rate (30 mm/yr), according to the NUVEL-1A plate motion model (DeMets et al., 1994). GPS data show that about half of the convergence is taken up by the ZFTB, and indicates that crustal shortening over ~450 km along the ZFTB decreases steadily from 9 mm/yr in the southeastern section to 7 mm/yr and 4 mm/yr in central and northwestern Zagros, respectively (Vernant et al., 2004; Reilinger et al., 2006). The instrumental seismicity rate increases significantly from NW to SE of the Zagros (Nissen et al., 2011). Recent studies show that nearly all earthquakes generated on the segmented reverse Mountain Front Fault nucleate depths shallower than 20 km (Talebian and Jackson, 2004).

On 12 November 2017, a strong earthquake with Mw 7.3 struck in the border region between Iran and Iraq near the province of Kermanshah, Iran (hereafter referred to as the 2017 Sarpol Zahāb earthquake) (Fig. 1). The seismic event was widely felt in the western and central provinces in Iran. The earthquake caused over 630 casualties, thousands of injures, immense building damages and large economic losses (Ahmadi and Bazargan-Hejazi, 2018). Numerous landslides and rock falls were reported from field investigations. However, no coseismic surface ruptures associated with the seismogenic fault were observed in the field. The earthquake was preceded by at least three foreshocks of magnitude up to 4.5 and had over one thousand aftershocks with a maximum magnitude of 5.4 within one month after the mainshock. The focal mechanism solutions of the 2017 earthquake reported by the global and local earthquake catalogs (see in Fig. 1) suggest slightly oblique thrust faulting, that is, the seismogenic fault dips either shallowly to the west-northwest or steeply to southwest.

Space geodetic observations of coseismic ground deformation provide important data to investigate the seismogenic fault and the subsurface deformation mechanics. Barnhart et al. (2018) analyzed a series of Sentinel-1 data and inferred that the coseismic rupture occurred on a shallow dipping within the Arabian crystalline basement, while afterslip concentrated up dip of the rupture zoned on the basal decollement. Using similar geodetic data, Feng et al. (2018) found two large-slip asperities with a maximum slip of 6 m at ~15 km depth. In this study, we use both C-band Sentinel-1 and L-band ALOS-2 data with multiple viewing geometries to generate the coseismic ground deformation maps. We also use the high temporal resolution teleseismic data to

* Corresponding author.
E-mail address: wenbin.xu@polyu.edu.hk (W. Xu).

https://doi.org/10.1016/j.tecto.2018.09.015
Received 19 June 2018; Received in revised form 26 September 2018; Accepted 29 September 2018
Available online 04 October 2018

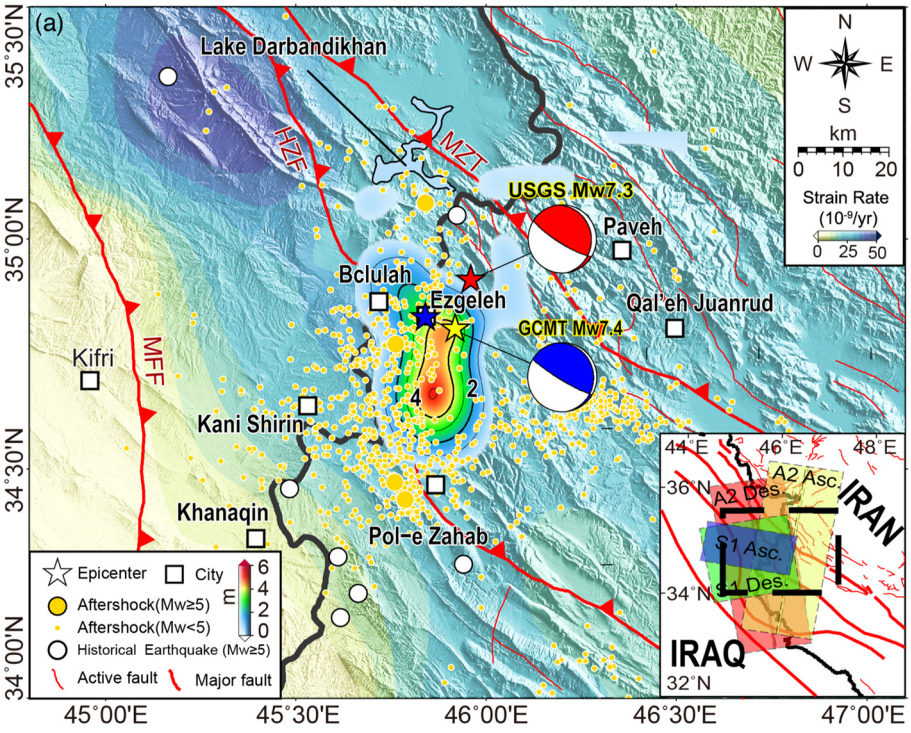

Fig. 1. (a). Location of the 2017 Sarpol Zahāb earthquake at the border between Iraq and Iran (black line). The color pattern shows total slip, estimated from the joint inversion of geodetic and seismic data. Background color shaded area represents the second invariant of the strain rate field in the study area (http://gsrm.unavco.org). Orange dots denote the aftershocks recorded by the Iranian Seismological Center (http://irsc.ut.ac.ir). Thick red lines denote the major faults in the region. The epicenter determined from different seismological agency is represented by the blue (GCMT) and red (USGS) star, respectively. The yellow star marks the epicenter used in our joint model. The inset shows the coverage of SAR data from different platforms and orbits. MFF, Mountain Front Fault; HZF, High Zagros Fault; MZT, Main Zagros Thrust (Mohajjel and Rasouli, 2014). (For interpretation of the references to colour in this figure legend, the reader is referred to the web version of this article.)

characterize the rupture process more comprehensively. Combing both geodetic and seismic data, we estimate final slip and the temporal slip evolution. Finally, we discuss the seismotectonic characteristics of the 2017 Sarpol Zahāb earthquake and interpret the source parameters and rupture process to better understand the architecture and kinematics of deformation in Zagros.

2. Data and inversion methods

We obtained ALOS-2 (L-band) and Sentinel-1 (C-band) SAR data from both ascending and descending orbits (Fig. 1). The ALOS-2 SAR images were acquired in the strip-map mode and the Sentinel-1 SAR images in the terrain observation with progressive scan (TOPS) mode (more detailed information of these SAR data can be found in Table S1). Given the size and depth of this event, surface deformation both near the epicenter and farther away is completely covered by these SAR data. Both the ALOS-2 and Sentinel-1 SAR data were processed using the GAMMA software. We followed a two-step coregistration method (Xu, 2017) to precisely align two Sentinel-1 TOPS data into the same grid. We used 1 arc-second digital elevation model of NASA's Shuttle Radar Topography Mission to remove the topographic contribution from the interferograms. The Goldstein adaptive filtering method was used to filter the noise in the interferograms and the minimum cost flow method was used to unwrap the filtered phase (Chen and Zebker, 2000). Finally, a total of four unwrapped coseismic interferograms were generated.

We selected and downloaded broadband teleseismic P-wave waveforms at 37 stations (Fig. 2) from the Incorporated Research Institutions for Seismology data center. The epicentral distances of these stations range from 30° to 90°. The distribution shows a good azimuthal coverage. After removing instrumental response, the digital records were converted to ground displacement waveforms, which were bandpass-filtered with corner frequencies of 0.005 to 0.4 Hz and then decimated to 1 Hz. A 60-s-long time window was extracted from the raw data, starting 6 s prior to the clearest first arrival of the P waves. The P wave initial motions were aligned manually to the theoretical arrival time based on the Preliminary Reference Earth Model (Dziewonski and Anderson, 1981).

In the modeling, we used the geodetic data to invert for the source geometry assuming a uniform-slip fault model, applying Okada (1985). We then discretized the fault into 15 sub-faults in the strike direction and 15 sub-faults in the dip direction with each fault patch covering $8 \times 8\,km^2$. The source time function of each sub-fault was parameterized with five symmetric triangles of 4 s half-durations, staggered by 2 s each. For each fault patch, two orthogonal slip vectors with rake angles of 90° and 180° were used. The non-negative least square inversion was employed to allow for the estimation of a rake-varying slip (Hartzell et al., 2007) in order to test if the composite rake angle (λ) is consistent with the Global Centroid Moment Tensor (GCMT) solution ($\lambda = 140°$). The joint inversion involves the selection of relative weight for each data set, however, there is no obvious objective way to automatically determine optimal weights (Chen et al., 2018). Here, we first normalize InSAR and teleseismic data by their own Frobenius norm and assign equal weights to them; the weights will be adjusted to improve data fits which are initially poorly predicted. This trial-and-error procedure may be repeated until the fits to all datasets are the best possible.

We used a frequency-wavenumber integration method (Zhu and Rivera, 2002) to compute Green's functions for InSAR data based on the CRUST 2.0 (http://igppweb.ucsd.edu/~gabi/crust2.html) 1-D layered rigidity model (see Table S2). The teleseismic Green's functions were produced with a propagator matrix approach (Kikuchi and Kanamori, 1982). We adopted the CRUST 2.0 velocity model for the source side and preliminary reference Earth model (Dziewonski and Anderson, 1981) for the receiver side. The Green functions were bandpass filtered as the data, in the range [0.005, 0.4] Hz. We assume a maximum rupture velocity is 3.2 km/s for the first window, which corresponds to 80% of the shear wave speed of the deepest layer. To ensure the stability of the inversion result, we employed the first-order Laplacian regularization (Hartzell and Heaton, 1983) to constrain spatiotemporal rupture evolutions.

3. Results

The InSAR deformation patterns from ascending and descending orbits look similar, indicating that the vertical deformation is the

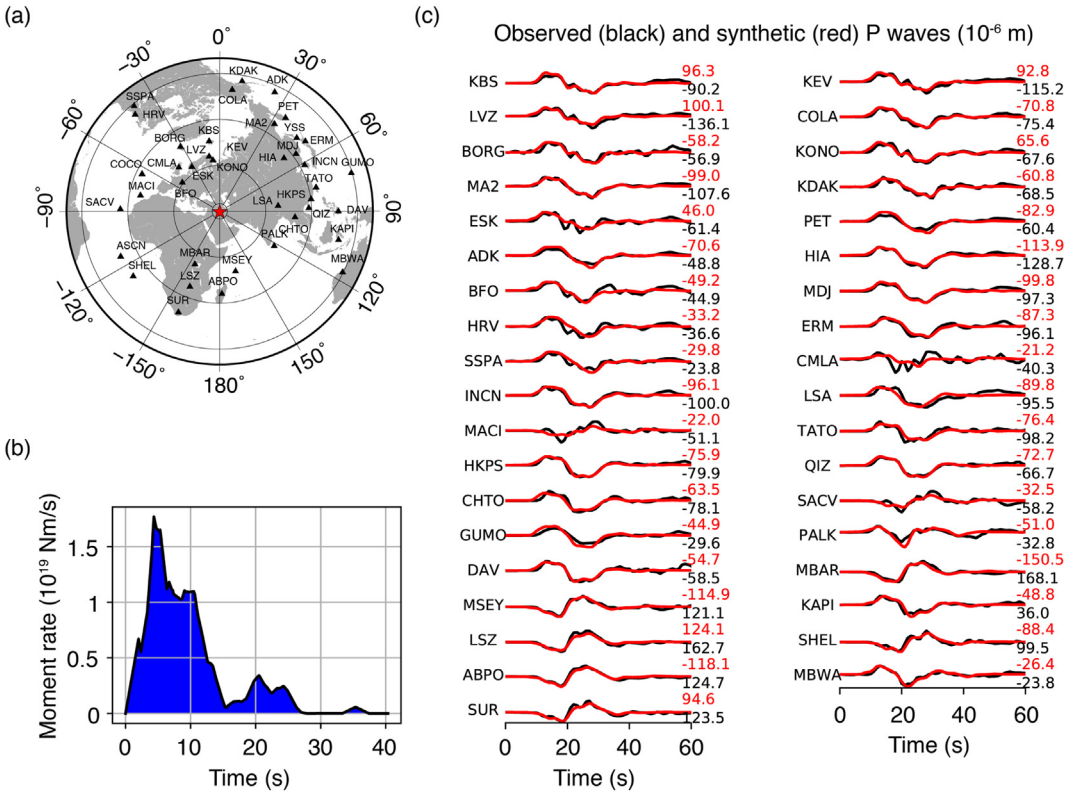

Fig. 2. P wave observations and fits for the joint model (a). Distribution of broadband seismic stations, the red star denotes the epicenter. (b). Moment rate function. (c). Comparison of observed P wave displacement waveforms (black) with fitted synthetic waveforms (red). Numbers to the right show the maximum amplitude for each waveform (units 10^{-6} m). (For interpretation of the references to colour in this figure legend, the reader is referred to the web version of this article.)

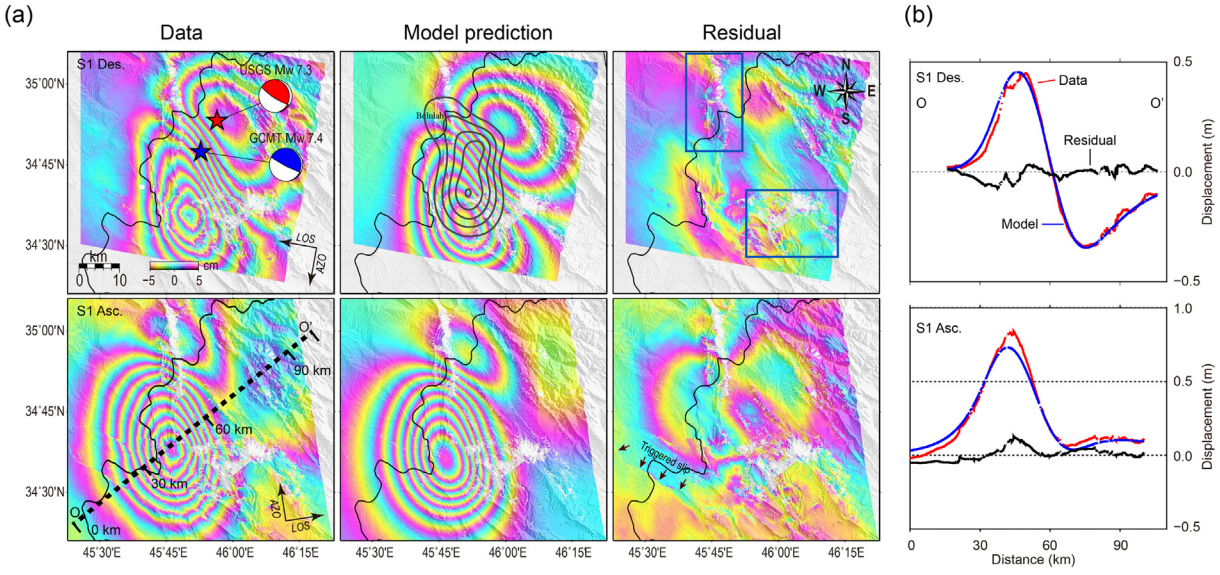

Fig. 3. (a). Coseismic InSAR displacement map from the descending (first row) and ascending (second row) Sentinel-1 data, model prediction based on our joint inversion slip model, and residuals. The stars denote the epicenter. (b) Profiles showing the observed and modeled displacements along section O-O′. The blue boxes outline the regions where most of the landslides have occurred. (For interpretation of the references to colour in this figure legend, the reader is referred to the web version of this article.)

dominant signal. The descending interferograms show over 50 cm uplift and about 30 cm subsidence in the radar line of sight (LOS) direction, respectively (Figs. 3 and 4). The ascending interferograms are dominated by a major uplift signal of about 90 cm in LOS (Figs. 3 and 4). As the LOS vector from the ascending orbit is nearly perpendicular to the strike of the seismogenic fault, the LOS motion in the ascending orbit reflects more vertical deformation than that in the descending orbit. We further decompose both ascending and descending data into vertical and horizontal surface displacements. We observe that the dominant signal is surface uplift of ~90 cm, while the horizontal ground deformation of up to 40 cm is distributed in a broader region. The smooth ground deformation field indicates that the majority of fault slip occurred at depth. The coherence of the interferograms is well maintained except in steep mountainous regions where landslides occurred. Careful

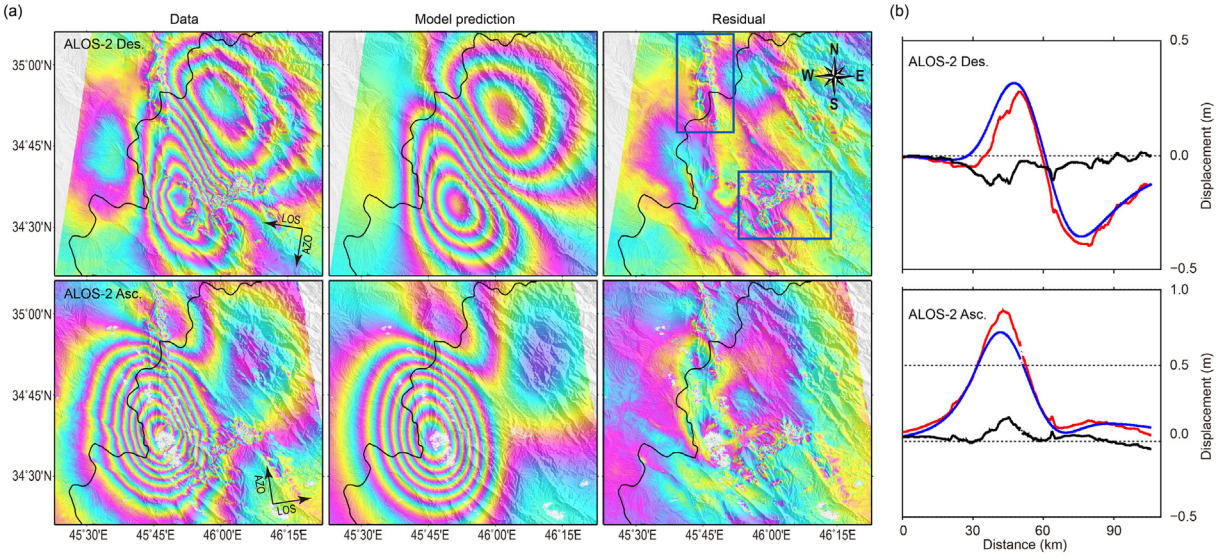

Fig. 4. Same as Fig. 3, but for descending (first row) and ascending (second row) ALOS-2 data.

inspections of the interferograms reveal clear discontinuities in phase at the surface (Figs. 3 and 4). These shallow surface fault movements are likely triggered by coseismic fault movements.

The preferred fault geometry based on geodetic observations favors a 15° west dipping fault, striking at 351°. This geometry is consistent with the GCMT fault plane solution. Note that the hypocenter locations (see Table S3) provided by the Iran Building and Housing Research Center (BHRC), Institute of Geophysics Tehran University (IGTU), and USGS are tens of kilometers from each other. Therefore, we test them one by one in the inversion, and find that the BHRC hypocenter location fits both InSAR and teleseismic waveforms best. For the joint inversion, we run 25 iterations with various spatial and temporal smoothing levels and choose the favoured one based on Akaike's Bayesian Information Criterion (ABIC, Sekiguchi et al., 2000), ABIC against different smoothing factors is depicted in Fig. S1. The joint inversion results show that the rupture zone of the main shock covers an area of ~40 km length, with slip being concentrated at depths between 13 and 20 km. The maximum slip of ~5 m is located at ~18 km south away from the town of Sarpol Zahāb. The total seismic moment is 1.35×10^{20} Nm, equivalent to Mw 7.39. As summarized in Table 1, our joint model overall agrees with InSAR-only model presented by Barnhart et al. (2018) and Feng et al. (2018), but our slip model also reproduces the major characteristics of the teleseismic waveforms (Fig. 2). The variance reduction of InSAR data and teleseismic waveforms of the best-fitting model is 84% and 76%, respectively. In addition, we tested different patch sizes (i.e., $5 \times 5\,km^2$ and $10 \times 10\,km^2$) and inverted InSAR data and teleseismic waveforms independently (Fig. S2). As expected, increasing patch size will produce a more smooth rupture model, but the main slip patterns remain unchanged. In particular, while the geodetic solution indicates that most of the slip occurred along-strike south of epicenter, the teleseismic waveforms yield a more compact and deeper slip distribution around the epicenter. As it is well recognized, teleseismic data have quite poor spatial resolution, and we believe that the geodetic solution is more reliable.

Table 1
Source parameters estimated from different studies.

Solution	Strike (°)	Dip (°)	Rake (°)	Major slip depth (km)	Total moment (Nm)
Barnhart et al. (2018)	350	15	128	~12-20	0.95×10^{20}
Feng et al. (2018)	351	14.5	136	~12–17	1.08×10^{20}
This study	351	15	135	~13–18	1.35×10^{20}

The spatiotemporal history of the earthquake rupture suggests a total rupture duration of ~25 s, with most of the seismic moment being released in the first 15 s (Fig. 2b). From the hypocenter, the rupture expands rapidly (~3.2 km/s) in the along-strike direction, but relatively slowly (~1.5 km/s) in the along-dip direction during the first 4 s (Fig. 5). The main large-slip asperity starts to rupture 4 s to 8 s after nucleation. During this process, the earthquake releases ~60% of the total seismic moment. From 8 s to 12 s, the moment release in the main asperity appears to decrease quickly. After 12 s, the earthquake rupture becomes much less energetic, with slip restricted to the largest slip zone (Figs. 5 and S3). Further details are contained in the local source-time function for each fault patch (Fig. S4).

To test the reliability of our modeling and to explore the resolution of the inverted slip, we conduct checkerboard tests (Fig. S5). In these tests, we fixed the fault geometry, smoothing factors, rupture speed and rise time length to our previously used values. We find that the teleseismic data recover the overall seismic moment release quite well, but not the distribution of slip. Applying the joint inversion of space geodetic data and seismic waveforms, both the input slip patterns and moment rate can be well retrieved at depths shallower than the hypocenter where significant slip occurred coseismically.

4. Discussion

Numerous segmented active blind thrust fault systems exist in the NW Zagros. The High Zagros fault and the Mountain Front fault are two major active thrust faults in the region, one of which is very likely to be responsible for the 2017 event. Studies of fault plane solutions of historical earthquakes on the Mountain Front fault show pure thrust-faulting events occurring at depths between 10 and 20 km (Engdahl et al., 2006). As the hypocenter of the 2017 event is located beneath the High Zagros fault at ~15 km depth, we can rule out the High Zagros fault to be the source fault. Extending the modeled fault plane to the surface, we find a possible fault surface trace that is located close to the Mountain Front fault in case the fault is listric (dip angle changes from shallow at greater depths to steep at shallower depths). In the Zagros, steeply dipping shallow faults widely exist as identified in regional structural studies (Molinaro et al., 2005) and account for small surface offsets (McQuarrie, 2004). Therefore, the 2017 event was a blind oblique-thrust faulting event on the deep section of the Mountain Front fault (Fig. 6). Our interpretation is consistent with Barnhart et al.

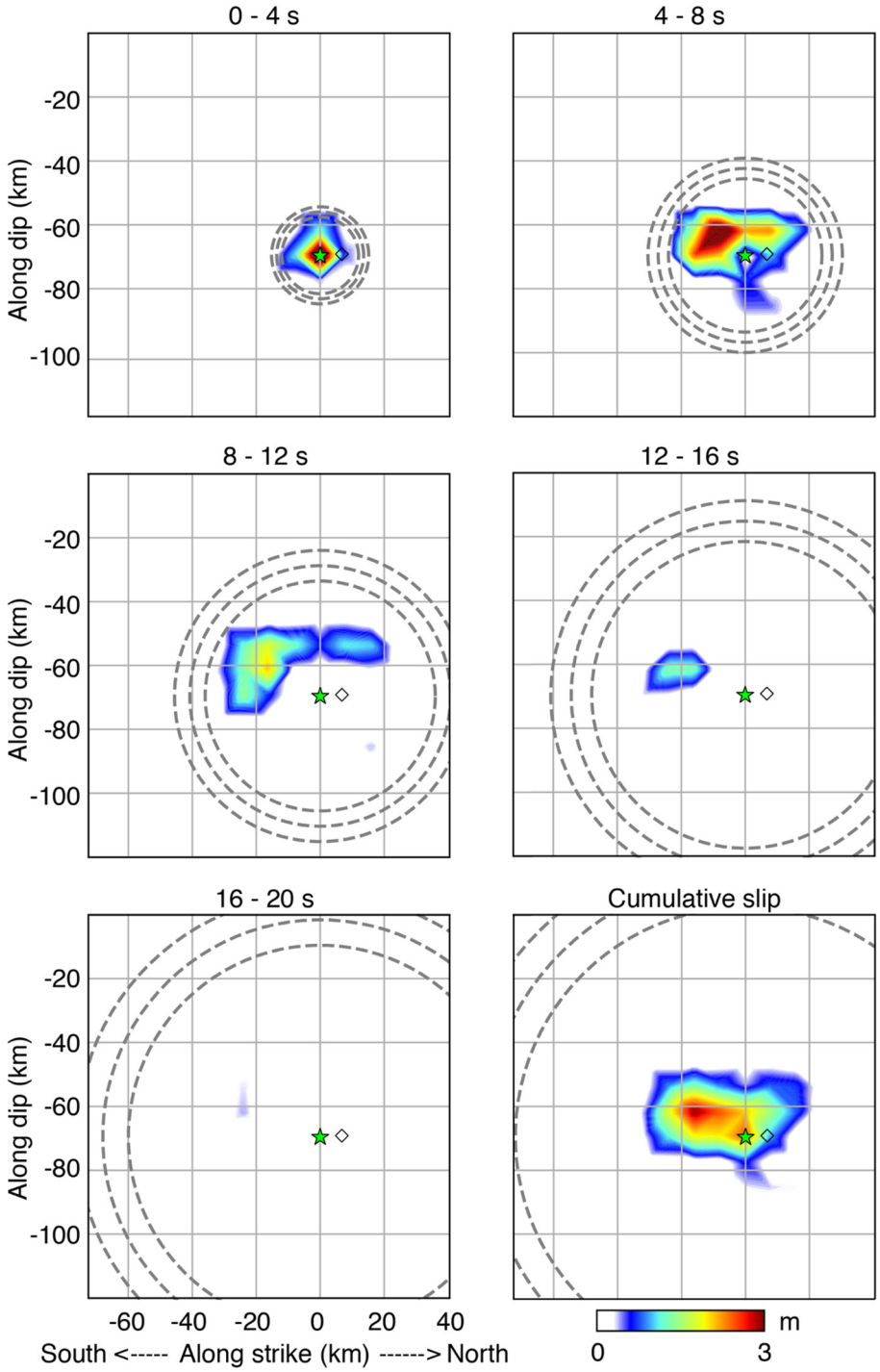

Fig. 5. Four-second snapshots of rupture propagation and amount of fault slip based on our joint inversion of teleseismic and geodetic datasets. The green star denotes the hypocenter and the diamond represents the GCMT centroid location, respectively. The grey dashed circles are the reference rupture fronts moving out at 3 km/s, 3.2 km/s, and 3.4 km/s, respectively. (For interpretation of the references to colour in this figure legend, the reader is referred to the web version of this article.)

(2018). In contrast, Feng et al. (2018), propagated their source model towards the surface and suggested that the Khanaqin fault to be the source fault.

Our preferred slip model shows an average rake angle (λ) of ~135° (see Fig. S6), which indicates that the magnitude of thrust slip component is as large as that of the left lateral strike slip. This type of fault motion is likely controlled by the present-day tectonic stress field in the region and the dynamics of the collision between the Arabian and Eurasian plates (Zoback, 1992; Reilinger et al., 2006). The world stress map shows that the epicenter is located in a regime where the maximum horizontal strike slip faulting stress is mixed with thrust faulting stress (Zoback, 1992). Tectonically, the Arabian plate is subducting underneath the Eurasian plate forming the Zagros mountains. A GPS station (ILAM) close to the epicenter shows that the northern part of the Arabian plate is rotating counterclockwise towards the NNW direction at a rate of ~18 mm/yr with respect to a fixed Eurasian plate (Reilinger et al., 2006). Oblique collision between the Arabian and Eurasian plates near the Iraq-Iran border favors oblique fault movements and slip

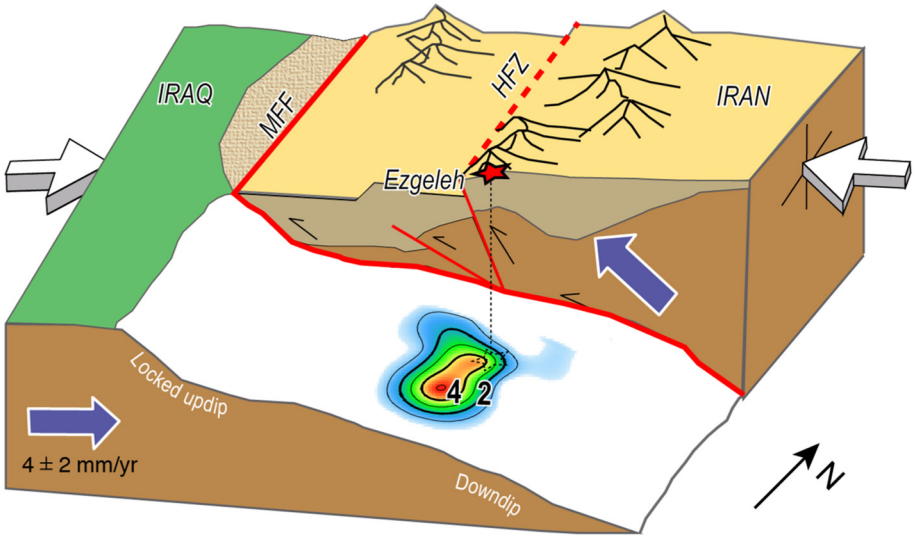

Fig. 6. A conceptual model showing the coseismic rupture with final slip colored and contoured (in meters) of the 2017 Sarpol Zahāb earthquake. The red star denotes the epicenter location. The blue arrows show the plate's moving directions. The white arrows represent the forces acting at the plate boundaries. Note that the figure is not to scale. (For interpretation of the references to colour in this figure legend, the reader is referred to the web version of this article.)

partitioning.

The recurrence time of large earthquakes is important for seismic hazard assessment. The large-slip asperity of the 2017 event is located in a zone of relatively high interseismic strain rate (Fig. 1). The coseismic slip at moderate depth represents the release of elastic strain accumulated in the middle crust during the interseismic phase. A quantitative analysis of over a century of historical earthquakes in the NW of Zagros shows that the seismic strain rate near the 2017 epicenter is relatively low ($\sim 4 \times 10^{-9}$ year^{-1}; Raeesi et al., 2017). The region around the 2017 epicenter is characterized by a low seismicity rate, a high b-value, and long mean return period of large events, in contrast to SE of the Zagros (Mousavi and Ebbing, 2018). This suggests that the causative fault system is mature enough to generate large earthquake in NW Zagros. The largest historical seismic event near the 2017 epicenter is unknown. The existing earthquake catalogs (USGS-NEIC and Iranian Seismological Center) show that very few $M > 5$ earthquakes are recorded since 1900 within a radius of 50 km around the 2017 epicenter. Assuming that the 2017 event has fully released the accumulated elastic strain on the fault segment and considering that a convergence rate of 4 ± 2 mm/yr (Vernant et al., 2004), we estimate that the recurrence time of the same causative fault segment for a Mw 7 event falls into the range between 600 and 1700 years. Barnhart et al. (2018) suggest a recurrence interval of $\geq$720 years, consistent with our findings. These estimates, however, do not fully account for the stress state and frictional property of the fault being the upper limit values.

Early aftershocks recorded by the Iranian Seismological Center and the estimated afterslip (Barnhart et al., 2018; Feng et al., 2018) are distributed in the along-strike direction and partially overlap with the coseismic slip in the up-dip segment within the sedimentary cover (Fig. 1). The occurrence of these aftershocks and afterslip are a response to coseismic stress perturbations. Few aftershocks are observed at the shallower depth (< 5 km) indicating that these sections of the seismogenic fault are locked. The absence of aftershocks at depth > 20 km is related to aseismic plastic flow in the continuous-quasi-plastic shear zone below the seismogenic zone and the Moho (Berberian, 1995) or due to the existence of a temperature transition zone as observed in other subduction zones (Hyndman and Wang, 1993). As these aftershocks are not relocated, their depths do not provide useful information in terms of whether these aftershocks occurred within the ruptured plane or shallower splay faults.

5. Conclusions

We have jointly used space geodetic and seismic data to study the source process of the 2017 Sarpol Zahāb earthquake in the northwestern end of the Zagros fold and thrust belt. The earthquake did not break the surface, but triggered a number of shallow fault slip and caused extensive landslides. We found that the 2017 event creates a single rupture asperity with a peak fault slip of ~5 m at ~15 km depth. The estimated seismic moment is 1.35×10^{20} Nm, corresponding to Mw 7.39. The 2017 event ruptured the deep portion of the Mountain Front fault affecting the uppermost basement and lowermost sedimentary cover. This is the largest instrumentally recorded event in the Zagros that did not break the entire seismogenic crust in one go. Large (and potentially larger) earthquakes might be expected across this region given the significant rate of strain accumulation across the entire area.

Acknowledgement

The authors thank editor Kelin Wang and two anonymous reviewers for comments that greatly improved this manuscript. The seismic data were processed using the SAC software packages. The ALOS-2 data were provided by JAXA (http://en.alospasco.com) under a contract of the 6th Research Announcement for ALOS-2 (No. P1246, P3381) and the Sentinel-1A data by ESA/Copernicus (https://scihub.copernicus.eu). Several figures were prepared by using the Generic Mapping Tools software. The modified Mudpy software was used for slip inversion. W. X. was supported by the Hong Kong Research Grants Council Early Career Scheme Fund (F-PP4B). P.M.M is funded by King Abdullah University of Science and Technology (KAUST) in Thuwal, Saudi Arabia, grants BAS/1339-01-01.

Appendix A. Supplementary data

Supplementary data to this article can be found online at https://doi.org/10.1016/j.tecto.2018.09.015.

References

Ahmadi, A., Bazargan-Hejazi, S., 2018. 2017 Kermanshah Earthquake: Lessons Learned. J. Inj. Violence Res. 10, 1–2.
Barnhart, W.D., Brengman, C.M.J., Li, S., Peterson, K.E., 2018. Ramp-flat basement structures of the Zagros Mountains inferred from co-seismic slip and afterslip of the 2017 Mw7.3 Darbandikhan, Iran/Iraq earthquake. Earth Planet. Sci. Lett. 496, 96–107.
Berberian, M., 1995. Master "blind" thrust faults hidden under the Zagros folds: active basement tectonics and surface morphotectonics. Tectonophysics 241, 193–224.
Chen, C.W., Zebker, H.A., 2000. Network approaches to two-dimensional phase unwrapping: Intractability and two new algorithms. J. Opt. Soc. Am. 17, 401–414.
Chen, K., Liu, Z., Liang, C., Song, Y.T., 2018. Towards the application of seismogeodesy in

central Italy: a case study for the 2016 August 24 Mw 6.1 Italy earthquake modelling. Geophys. J. Int. 213, 1647–1658.
DeMets, C., Gordon, R.G., Argus, D.F., Stein, S., 1994. Effect of recent revisions to the geomagnetic reversal time scale on estimates of current plate motions. Geophys. Res. Lett. 21, 2191–2194.
Dziewonski, A.M., Anderson, D.L., 1981. Preliminary reference Earth model. (PREM). Phys. Earth Planet. Inter. 25 (4), 297–356.
Engdahl, E.R., Jackson, J.A., Myers, S.C., Bergman, E.A., Priestley, K., 2006. Relocation and assessment of seismicity in the Iran region. Geophys. J. Int. 167, 761–778.
Feng, W., Samsonov, S., Almeida, R., Yassaghi, A., Li, J., Qiu, Q., Li, P., Zheng, W., 2018. Geodetic Constraints of the 2017 M w 7.3 Sarpol Zahab, Iran Earthquake, and its implications on the structure and mechanics of the Northwest Zagros Thrust-Fold Belt. Geophys. Res. Lett. 45, 6853–6861.
Hartzell, S.H., Heaton, T.H., 1983. Inversion of strong ground motion and teleseismic waveform data for the fault rupture history of the 1979 Imperial Valley, California, earthquake. Bull. Seismol. Soc. Am. 73 (6A), 1553–1583.
Hartzell, S., Pengcheng, L., Mendoza, C., Chen, J., Larson, K.M., 2007. Stability and uncertainty of finite-fault slip inversions: application to the 2004 Parkfield, California, earthquake. Bull. Seismol. Soc. Am. 97, 1911–1934.
Hyndman, R.D., Wang, K., 1993. Thermal constraints on the zone of major thrust earthquake failure: the Cascadia Subduction Zone. J. Geophys. Res. 98 (B2), 2039–2060.
Kikuchi, M., Kanamori, H., 1982. Inversion of complex body waves. Bull. Seismol. Soc. Am. 72, 491–506.
McQuarrie, N., 2004. Crustal scale geometry of Zagros fold-thrust belt, Iran. J. Struct. Geol. 519–535.
Mohajjel, M., Rasouli, A., 2014. Structural evidence for superposition of transtension on transpression in the Zagros collision zone: main recent Fault, Piranshahr area, NW Iran. J. Struct. Geol. 62, 65–79.
Molinaro, M., Leturmy, P., Guezou, J.-C., Frizon de Lamotte, D., Eshraghi, S.A., 2005. The structure and kinematics of the southeastern Zagros fold-thrust belt, Iran: from thin-skinned to thick-skinned tectonics. Tectonics 24, TC3007.
Mousavi, N., Ebbing, J., 2018. Basement characterization and crustal structure beneath the Arabia–Eurasia collision (Iran): a combined gravity and magnetic study. Tectonophysics 731-732, 155–171.
Nissen, E., Tatar, M., Jackson, J.A., Allen, M.B., 2011. New views on earthquake faulting in the Zagros fold-and-thrust belt of Iran. Geophys. J. Int. 186, 928–944.
Okada, Y., 1985. Surface deformation due to shear and tensile faults in a half-space. Bull. Seismol. Soc. Am. 75 (4), 1135–1154.
Raeesi, M., Zarifi, Z., Nilfouroushan, F., Boroujeni, S.A., Tiampo, K., 2017. Quantitative analysis of seismicity in Iran. Pure Appl. Geophys. 174, 793. https://doi.org/10.1007/s00024-016-1435-4.
Reilinger, R., et al., 2006. GPS constraints on continental deformation in the Africa-Arabia-Eurasia continental collision zone and implications for the dynamics of plate interactions. J. Geophys. Res. 111, B05411.
Sekiguchi, H., Irikura, K., Iwata, T., 2000. Fault Geometry at the Rupture termination of the 1995 Hyogo-ken Nanbu Earthquake. Bull. Seismol. Soc. Am. 90, 117–133. https://doi.org/10.1785/0119990027.
Talebian, M., Jackson, J., 2004. A reappraisal of earthquake focal mechanisms and active shortening in the Zagros mountains of Iran. Geophys. J. Int. 156, 506–526.
Vernant, P., et al., 2004. Present-day crustal deformation and plate kinematics in the Middle East constrained by GPS measurements in Iran and northern Oman. Geophys. J. Int. 157, 381–398.
Xu, W., 2017. Finite-fault slip model of the 2016 M_w 7.5 Chiloé earthquake, southern Chile, estimated from Sentinel-1 data. Geophys. Res. Lett. 44, 4774–4780.
Zhu, L., Rivera, L.A., 2002. A note on the dynamic and static displacements from a point source in multilayered media. Geophys. J. Int. 148, 619–627.
Zoback, M.L., 1992. First-and second-order patterns of stress in the lithosphere: the World Stress Map Project. J. Geophys. Res. 97 (B8), 11703–11728.